*Article*

# Melting of Paraffin Waxes Embedded in a Porous Matrix Made by Additive Manufacturing

**Andrea Diani *** [ID]**, Lorenzo Moro and Luisa Rossetto** [ID]

Department of Industrial Engineering, University of Padova, Via Venezia 1, 35131 Padova, Italy;
lorenzo.moro@unipd.it (L.M.); luisa.rossetto@unipd.it (L.R.)
* Correspondence: andrea.diani@unipd.it; Tel.: +39-049-8276893

**Abstract:** The recent advances in additive manufacturing technology have widened the choice of materials that can be printed, opening new frontiers in the field of heat transfer devices. This paper explores the use of a solid porous matrix in which paraffin waxes, having different melting temperatures (42, 55, and 64 °C), were embedded. The solid matrix is made by additive manufacturing. The parent cell of the porous matrix occupies the volume of a cube with an edge of 5 mm. The entire 3D printed matrix has a square base with an edge of 100 mm, and it has a height of 20 mm. The solid matrix was printed between two plates, each one with a thickness of 10 mm, where thermocouples were inserted, and it was tested in an upright position, laterally heated applying three different heat fluxes (10, 15, and 20 kW m$^{-2}$). The experimental results are given in terms of the temperature of the heated side, as well as of the phase change material, during the heating process. The temperature reached by the heated side and the time needed to completely melt the paraffin waxes are compared at the different working conditions. Furthermore, the thermal conductivities and diffusivities of the three paraffins and of the parent material of the porous matrix were experimentally evaluated.

**Keywords:** PCM; paraffin; additive manufacturing; temperature profile; BCC model

## 1. Introduction

Additive manufacturing (AM) is a technology that permits the construction of a tridimensional object starting from CAD models. The actual state of the art of this technology has widened the choice of materials to be printed, opening new frontiers for heat transfer devices: not only plastic materials can now be printed, but also metallic materials, with consequent higher thermal conductivities. Many different fields of thermal sciences can have benefits for single- or two-phase applications. Kwon et al. [1] studied a way to enhance the heat transfer during liquid water cooling of a horizontal heated plate by means of static mixers made by additive manufacturing. Two different types of mixing devices were considered: twisted tape structures and chevron-shaped offset wings. Both the structures improved the heat transfer coefficient by two times compared to the plain channel for Reynolds numbers below 1000.

Rastan et al. [2] investigated the feasibility of additive manufacturing to fabricate mini channel heat exchangers with longitudinal vortex generators. At a Reynolds number of 1380, the convective heat transfer coefficient can be up to three times that of the smooth channel, using distilled water as working fluid.

Unger et al. [3] experimentally tested tube bundles with conventional circular plain fins as well as new circular integrated pin fins and serrated integrated pin fins made by additive manufacturing during air forced convection with Reynolds number from 1600 to 6600. Fins with the new design demonstrated an improved Nusselt number compared to the conventional fins. Furthermore, the friction factor for the serrated integrated pin fins was the lowest for all the tested Reynolds numbers, and the circular integrated pin fins provided a lower friction factor compared to the conventional circular pin fins for Reynolds number lower than 4000.

Another research field where additive manufacturing can exploit its benefits is related to two-phase heat transfer systems, which involve a phase transition of a material from solid to liquid or vice versa. These materials, named PCMs (phase change materials), are usually characterized by a low thermal conductivity, which may degrade the heat transfer characteristics. Thus, PCMs are often coupled with a solid insert to enhance the thermal conductivity of the block. Different ways to enhance the thermal conductivity of PCMs have been proposed in the literature. Fok et al. [4] conducted an experimental study using n-eicosane as PCM embedded in a heat sink with and without internal fins for cooling portable hand-held electronic devices. Experimental results indicated that internal fins aided in lowering the temperature of the electronic device, and a higher number of fins revealed a lower temperature. A not appreciable effect of the orientation of the heat sink was observed. Baby and Balaji [5] carried out an experimental study to characterize the thermal performance of pin-finned heat sinks implementing paraffin wax and n-eicosane as PCMs. A configuration with only PCM was tested, as well as configurations with 33, 72, and 120 pins. The best thermal performance was given by the heat sink with 72 pins.

Another way to enhance the thermal conductivity of PCM is by using metal foams, which are cellular materials with randomly oriented fibers that form cells. Depending on the porosity, these cells can be open for high values of porosities. The parent material is usually characterized by a high thermal conductivity, thus increasing the overall conductivity. Among the first works related to PCM melting inside metal foams, Lafdi et al. [6] experimentally tested aluminum foams having 5, 10, 20, and 40 PPI (pores per inch), with porosities ranging between 0.886 and 0.966, coupled with paraffin waxes having melting temperatures from 25.4 to 28.9 °C. The heater temperature was lower in the case with foam having lower porosities, whereas the effect of the number of pores was minor. Zhou and Zhao [7] presented an experimental study on the phase change process of paraffin, as well as of calcium chloride hexahydrate, as PCMs embedded in metal foams and in expanded graphite. Experimental results revealed that the addition of a porous insert, either metal foam or expanded graphite, can enhance the heat transfer rate of the PCM. Other works related to the melting of PCM embedded in metal foams can be found in [8–12].

Instead of random structures, which are typical of metal foams, periodic structures can be generated by means of additive manufacturing technology, allowing the choice of every single detail of the sample to be printed. Different structures, such as Kelvin cells, Weaire-Phelan cells, or body-centered or face-centered cubic (BCC or FCC) cells, were reported in the literature to simulate the random structure of foams. Most of these studies were numerically carried out. Sinn et al. [13] carried out CFD simulations of conjugate heat transfer considering five periodic foams represented by Kelvin cell-lattice structures to be used as catalyst carrier, and they found that the strut diameter and the solid thermal conductivity were the key parameters to improve heat transfer and to reduce hot spots. Lucci et al. [14] compared CFD results of pressure drop and mass transfer coefficient of structures made by Kelvin cells and by micro-computed tomography scans of open-cell foams. Based on the numerical results, the authors demonstrated that Kelvin cells were a valid model to study real foams for porosities higher than 80%; in addition, Kelvin cells had clearly more favorable mass transfer to pressure drop trade-off. Other numerical studies of Kelvin cell structures can be found in [15–17].

The Weaire-Phelan model was considered by Kuruneru et al. [18], who numerically investigated non-isothermal solid-gas flows through an idealized metal foam heat exchanger, proving that the Weaire-Phelan model can be used as an alternative to the real metal foam sample. The Weaire-Phelan model was implemented by Yao and Wu [19] to simulate the melting phase change of paraffins at the pore-scale with volume change in high porosity open-cell foams.

BCC based structures were initially studied by Krishnan et al. [20], who computed the fluid and heat flow in BCC periodic structures, obtaining the effective thermal conductivity, pressure drop, and heat transfer coefficient. The numerical results were compared against existing experimental measurements and semiempirical models based on data related

to metal foams. Later on, the same authors [21] extended the study to other structures, such as FCC and A15 structures. A numerical study aimed at investigating the melting of paraffins inside a BCC structure was carried out by Ferfera et al. [22]. The numerical model was validated with experimental values from the literature. The results indicated that the decrease in the porosity resulted in an increase in the effective thermal conductivity of the metal foam, which makes the heat diffusion in the composite material faster than that in pure paraffin. Furthermore, a small pore diameter well uniformed the melting front and the temperature inside the composite structure.

As it can be noticed from this introduction, many of the works related to periodic structures are numerically conducted, and no experimental work on periodic structures similar to those previously reported can be found in the open literature. However, the recent developments in additive manufacturing (AM) technology permit the creation of periodic structures from CAD models, making possible experimental tests besides numerical simulations. This paper reports some experimental results on the melting of three different paraffin waxes, namely RT42, RT55, and RT64HC, inside a modified BCC structure with a base cell having an edge of 5 mm. The entire periodic structure has a square edge of 100 mm, and a thickness of 20 mm, and it is tested in an upright position. The structure was printed between two 10 mm thick plates, and it is laterally heated from one side. Results are given in terms of temperature profiles of the heated side, as well as of the PCM, during the heating process, coupled with visualizations that provide information on how the melting front of the PCM propagates. In the end, a comparison between the modified BCC structure and two metal foams is reported.

## 2. Porous Matrix

The porous matrix, inside which paraffins were embedded, was printed at LAMA FVG Lab. The technique Selective Laser Melting (SLM) was implemented for additive manufacturing. The matrix is made of $AlSi_{10}Mg$, which is an aluminum alloy.

The porous matrix is made of the repetition of base cells defined as body-centered cubic (BCC). The BCC structure derives from chemistry: the BCC crystal structure is a way for atoms to arrange themselves in metals. In this structure, eight atoms are located at the vertices of a cube, and one atom is in the middle of the cube. This idea can be taken to create cells that can form periodic cellular structures. In this concept, a cube with eight spheres located at the vertices and one sphere in the middle of the cube is considered. If the spheres have a radius that is greater than half of the edge of the cube, the subtraction between the volume occupied by the cube and the volume occupied by the nine spheres gives, as a result, a structure such as that reported in Figure 1a. In the proposed structure, the base cube has an edge of 5 mm. Since, as can be seen in the figure, the BCC structure presents very thin edges, which cannot be printed with AM technology, these thin edges were thickened in such a way that the thinnest edge was 0.4 mm, which is a value compatible with the SLM printer. The so-created modified BCC structure is reported in Figure 1b, and it represents the base element the entire structure is made of. This structure has a porosity, intended as the ratio between the volume occupied by the empty spaces and the total volume (solid matrix and empty spaces), of 0.87. A lateral view of the modified BCC structure is reported in Figure 1c, along with the dimensions.

This modified BCC structure tends to overcome the limits regarding porosity exploited by metal foams. As stated by Zhao [23], open-celled metal foams are considered as one of the most promising classes of materials to be used to enhance the transfer with phase change materials due to their high thermal conductivities and high heat transfer areas per unit of volume. Taking, for instance, Duocel® foams, due to the physics of small-scale structures, the majority of Duocel® foams are manufactured in the 90–97% porosity range. The proposed modified BCC structure overcomes this limit about porosity: AM technology permits the creation of periodic cells with porosities lower than those of metal foams guaranteeing open cells, which are needed to be filled with the PCM, avoiding any close cells that would be detrimental for the heat transfer mechanisms.
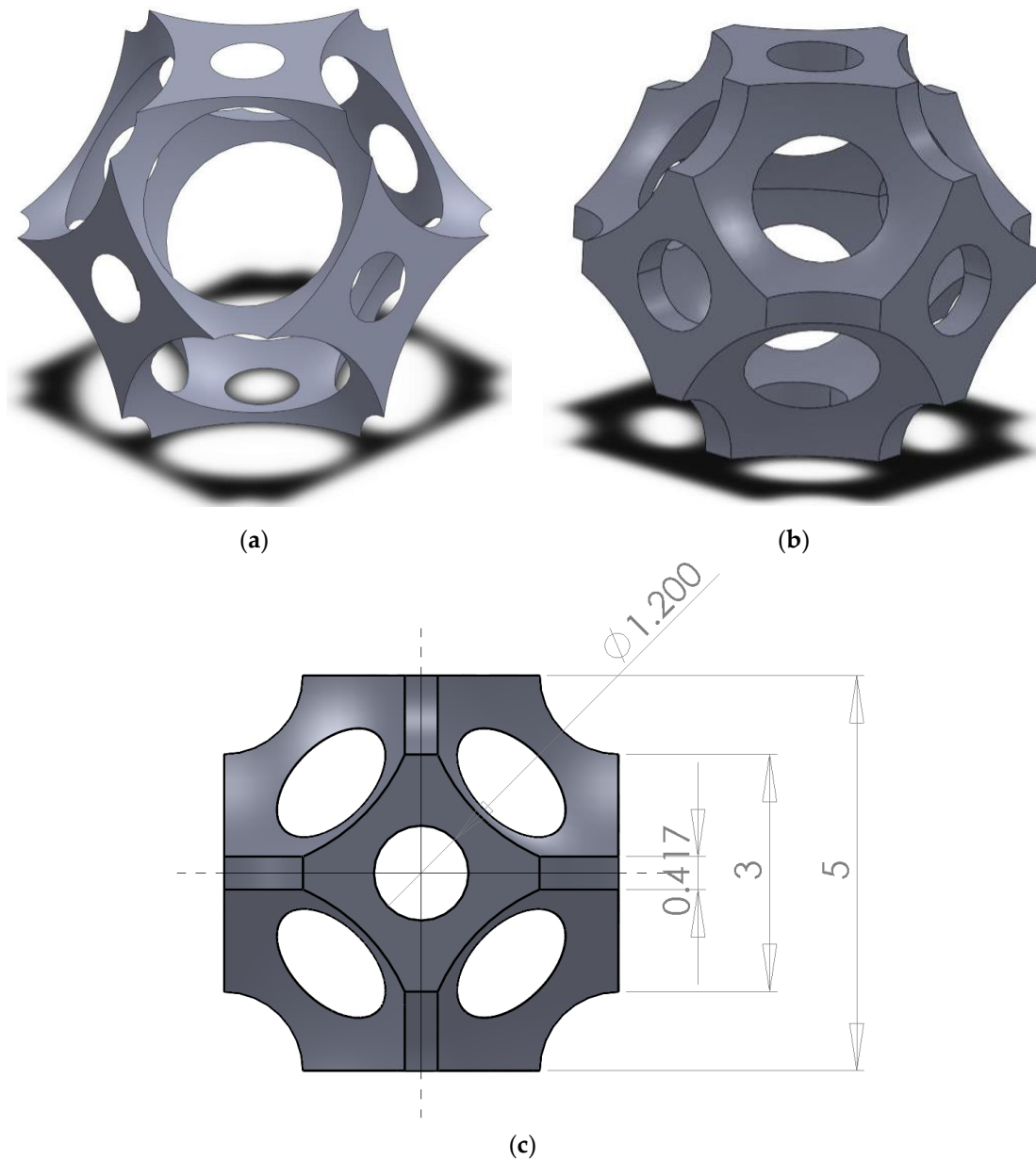
**Figure 1.** (**a**) BCC structure; (**b**) modified BCC structure; (**c**) lateral view of the modified BCC structure with dimensions.

The entire structure is made by the repetition of the modified BCC structure, and it has a volume of $100 \times 100 \times 20$ mm$^3$, i.e., the base cell is replicated 20 times along two coordinates and four times along the third coordinate. Furthermore, the final structure was printed between two 10 mm thick plates made of the same material. Since the structure was printed all together, there are no thermal resistances between the porous matrix and the two plates. Figure 2 shows a schematic of the entire structure. Six holes were drilled in each of the plates to host as many T-type thermocouples to monitor the wall temperature during the heating process. The location of these thermocouples is similar to that reported in Diani and Campanale [24], to which reference should be made for further details.
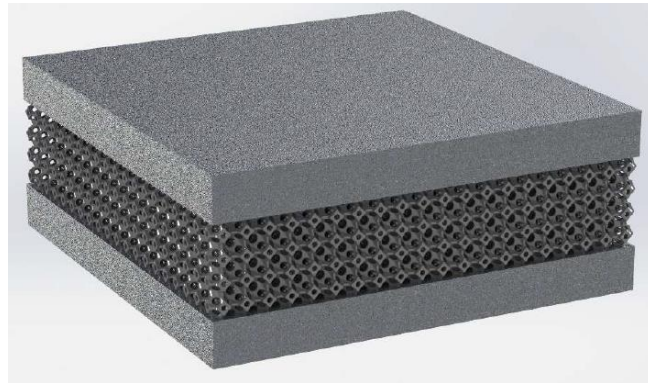
**Figure 2.** Porous matrix made by modified BCC cells between the two plates.

## 3. Test Module and Paraffin Waxes

The structure was experimentally tested in an upright position. The module was laterally heated by means of an electrical heater, which is a copper plate inside which a nickel-chrome wire resistance was inserted. This heater is placed in contact with one of the two plates of the structure, and a thermal paste was used between the heater and the plate. The heater is connected to a DC power supplier. Three different heat fluxes are supplied: 10, 15, and 20 kW m$^{-2}$, to which heat flow rates of 100, 150, and 200 W correspond. The supplied heat flow rate is calculated as the product between the electrical differential potential (EDP) across the heater and the current flowing into the heater. The EDP is directly measured, whereas the current is measured by means of a reference electrical resistance (shunt). The shunt is in series with the heater, and the measurement of the EDP across the shunt (whose resistance is known) permits the calculation of the current flowing in the electrical circuit. The supplied electrical power can be measured with such a technique with an uncertainty of $\pm$0.13%.

Two bakelite plates were glued to the structure, one to the bottom side and one to the rear side, and they act both as an insulating material and as containment for the paraffin. A glass window is glued to the front side, acting as containment and as a window to observe the melting front during the experimental tests. A schematic is reported in Figure 3a.



(**a**)

(**b**)
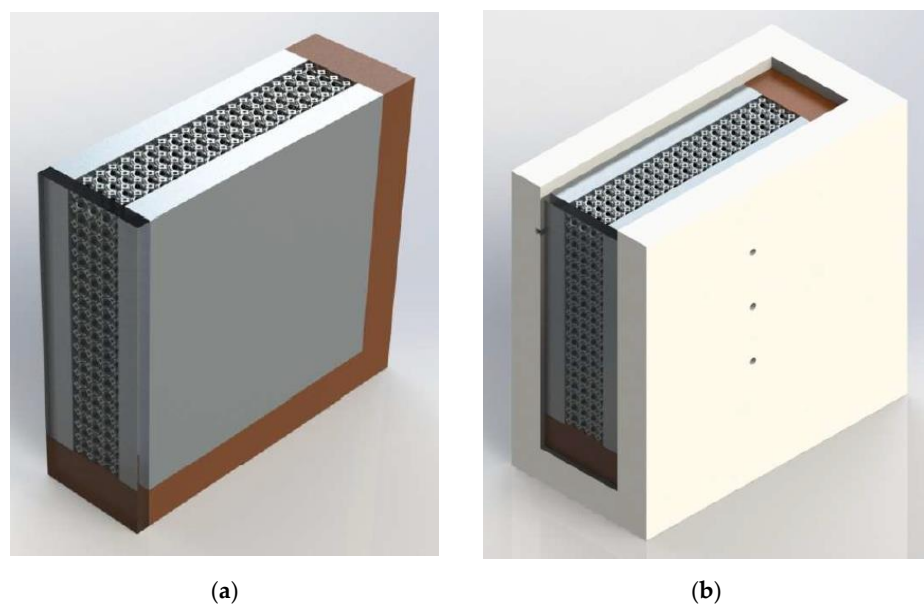
**Figure 3.** (**a**) Structure with bakelite plates and glass window; (**b**) entire module inside the Teflon case.

The entire module with the heater is placed inside a Teflon case (see Figure 3b) to limit as much as possible the heat losses to the external ambient. The top part is not covered to permit the filling procedure of the paraffin.

Three holes were drilled in the right plate, and thus also in the Teflon case, as reported in Figure 3b: these holes permit us to host three T-type thermocouples that measure the temperature of the paraffin inside the structure. The tips of these thermocouples reach the centerline in the middle of the porous matrix at 25, 50, and 75 mm from the bottom side of the structure. These thermocouples have an uncertainty of $\pm 0.5$ K. All the implemented thermocouples are connected to a Kaye 170 ice point temperature. All the signals, i.e., of the thermocouples and of the two EDP measurements, are connected to the data acquisition system (DAQ).

Three different paraffins were implemented for the experimental tests as phase change material. These paraffins have different melting temperatures, allowing us to understand the effect of this parameter on the thermal performance during the heating process. The paraffins have melting temperatures of 42, 55, and 64 °C, whose values are compatible with electronics cooling applications. The paraffins are named RT42, RT55, and RT64HC, and the number that appears in each name represents the correspondent melting temperature, even if it would be better to consider a melting temperature range instead of a specific melting temperature. These paraffins, supplied by Rubitherm GmbH, are chemically inert and stable after multiple cycles of melting and solidification. Some of the main thermophysical properties are reported in Table 1.

**Table 1.** Thermophysical characteristics of the tested paraffins. Data by the manufacturer [25].

|  | RT42 | RT55 | RT64HC | |
| --- | --- | --- | --- | --- |
| Melting temperature range | 38–43 | 51–57 | 63–65 | [°C] |
| Heat storage capacity [a] | 165 | 170 | 250 | [kJ kg$^{-1}$] |
| Density solid [b] | 0.88 | 0.88 | 0.88 | [kg dm$^{-3}$] |
| Density liquid [c] | 0.76 | 0.77 | 0.78 | [kg dm$^{-3}$] |

[a] combination of latent and sensible heat in a temperature range of 35 °C to 50 °C for RT42, of 48 °C and 63 °C for RT55, of 57 °C and 72 °C for RT64HC. [b] evaluated at 15 °C for RT42 and RT55, at 20 °C for RT64HC. [c] evaluated at 80 °C.

## 4. Measurements of Thermal Conductivities and Thermal Diffusivities

The thermal conductivities and thermal diffusivities of the three paraffins in the solid state, as well as of the AlSi$_{10}$Mg alloy sample, have been experimentally measured. Moreover, the knowledge of the density, $\rho$, permitted to calculate the specific heat, $c$, as:

$$c = \frac{k}{\rho \cdot a} \tag{1}$$

where $k$ is the thermal conductivity and $a$ is the thermal diffusivity.

The hot disk transient plane source (TPS) method was applied to measure thermal conductivity and thermal diffusivity. This is a transient type technique for the measurement of thermal conductivity. The measuring equipment was the commercial thermal constants analyzer model TPS 2500 HOT DISK AB. The hot disk method uses a flat sensor element in the shape of a double spiral that has been etched out of a thin nickel foil. The sensor is covered on both sides with two layers of electrically insulating film (kapton or mica). The kapton sensor provides an accuracy of $3 \div 5\%$, while the mica sensor provides lower accuracy (about $8 \div 10\%$) when measuring the thermal conductivity. During the measurements, the hot disk sensor is sandwiched between two sample halves of the specimen to be investigated, each one with a plane surface facing the sensor, as illustrated in Figure 4.
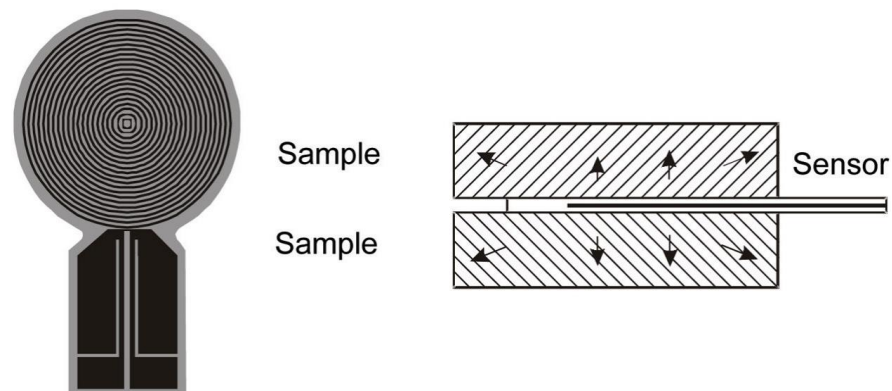
**Figure 4.** Hot disk sensor and sample.

The sensor acts both as a heat source for increasing the temperature of the sample and a resistance thermometer for recording the time-dependent temperature increase. During the experiment, constant electric power is supplied to the hot disk sensor. This causes the temperature to rise and an increase in the resistance of the spiral while the heat is absorbed by the test sample. This temperature increase is dependent on the thermal transport properties of the material surrounding the sensor. By monitoring this temperature increase over a short period of time after the start of the experiment, it is possible to evaluate the thermal properties of the material.

The ideal model of the heat conduction equation assumes that the sample can be considered as a semi-infinite medium during the time $t$ of measurement. However, being the samples of finite dimensions, this entails that the time of transient recording has to be chosen so that the outer boundaries of the sample do not influence the temperature increase detected by the sensor. In practice, by choosing short time intervals and proper sensor and sample sizes, the measurement can still be analyzed as if it was performed in an infinite medium. In this case, by fitting the theoretical solution of the variations of temperature of the specimen active surfaces to the experimental recorded temperature variations, using least-squares analysis, it is possible to calculate the thermal conductivity and the diffusivity of the tested material in an independent way. More details about this technique can be found in the references [26,27].

Four different materials were studied: three paraffins and an $AlSi_{10}Mg$ alloy sample. Table 2 lists the materials and experimental results. The thermal conductivities of all samples were measured at room temperature (23 °C). The presented values are the mean of at least five repeated measurements with the same test setup and boundary conditions. The relative standard deviation of repeated thermal conductivity measurements has been less than 1.2% for all samples. A kapton sensor with a 9.868 mm radius was used for the paraffins and a kapton sensor with a 3.189 mm radius for the $AlSi_{10}Mg$ alloy sample. The electrical power and time interval were set at $P = 20.65$ mW, $t = 160$ s for the paraffins and $P = 450$ mW, $t = 1$ s for $AlSi_{10}Mg$ alloy sample. The specific heats, reported in Table 2, are derived from Equation (1).

**Table 2.** Measured characteristics of the tested paraffins and of $AlSi_{10}Mg$.

|  | RT42 | RT55 | RT64HC | $AlSi_{10}Mg$ |  |
|---|---|---|---|---|---|
| Thermal conductivity | 0.27 | 0.27 | 0.34 | 175 | [W m$^{-1}$ K$^{-1}$] |
| Thermal diffusivity | 0.169 | 0.152 | 0.250 | 73.8 | [mm$^2$ s$^{-1}$] |
| Specific heat | 1805 | 1999 | 1555 | 870 | [J kg$^{-1}$ K$^{-1}$] |

## 5. Experimental Results

### 5.1. Preliminary Considerations

The porous structure was tested with three paraffins, and each paraffin was tested with three different applied heat fluxes, and so the effect of both melting temperature of

the paraffin and of heat flux can be depicted. Experimental results will be given in terms of the temperature profile of the plate in contact with the heater and the temperature profile of the PCM at the three different locations during the heating process.

The first step is the filling of the porous matrix with the paraffin wax: once the structure was heated up to a temperature higher than the melting temperature of the paraffin, the paraffin is poured in the liquid phase, and the filling is deemed concluded as soon as the entire structure is embedded with liquid paraffin. The test module is left to cool down up to ambient temperature, i.e., the experimental tests start at ambient temperature. Due to the volume contraction from liquid to solid state, the solid paraffin does not fill the entire porous matrix: this choice was taken in order to prevent any leakage due to volume variation during the heating process.

The data acquisition system (DAQ) is switched on as soon as the DC power supplier is turned on, and the DAQ is set at a frequency of 1 Hz. Since tests start at ambient temperature, the values of temperature recorded at $t = 0$ s correspond to the ambient temperature. Each experimental test is deemed concluded as soon as all the PCM is completely melted inside the porous structure. The temperature of the heated side, as well as the temperature of the phase change material, are recorded. Furthermore, pictures of the melting front were taken from the glass window, and they permit us to understand how the melting front propagates inside the paraffin.

*5.2. Common Characteristics of the Melting Process*

Figure 5 shows the temperature profiles during the heating process for the case with the paraffin RT42 with an imposed heat flux of 10 kW m$^{-2}$. The red line represents the temperature of the plate in contact with the heater, i.e., it represents the temperature of the heated side. Since the temperatures recorded by the six thermocouples located in the heated side are within ±1.2 K at each time during the heating process, the average value of temperature is considered in the figure. After just a few seconds, during which the electric power is set to 100 W, the temperature of the heated side increases almost linearly when only sensible heat is involved in the heating process. As soon as the temperature of the heating side approaches the low value of the melting temperature range, the paraffin close to the heated plate starts to melt; thus, the slope of the curve of the temperature of the heated side decreases, i.e., latent heat is also involved. The green, blue and gray lines represent the temperatures of the phase change material in the centerline at different heights: 25, 50, and 75 mm from the top side, respectively. As it can be noticed from Figure 5, these three lines almost overlap, meaning that there is no temperature gradient along the height of the paraffin. This may indicate that the melting front is moving quite parallel to the heated surface. The curves related to the temperatures of the PCM present two changes of slope: the first one is in correspondence with the lower value of the melting temperature range, whereas the second one is in correspondence with the upper value of the melting temperature range. The temperature of the paraffin during the phase change process from solid to liquid state is not constant since the melting occurs in a temperature interval (38–43 °C in the case of RT42). Similar conclusions can be depicted for the other combinations of heat flux and paraffin: each experimental test will have different temperatures of the heated side at the end of the heating process as well as different times needed to completely melt the paraffin, as it can be seen in Table 3. The table reports the values of $T_i$, $T_f$, and $t_{melt}$, which are, respectively, the initial temperature of the heated side, the temperature of the heated side at the end of the melting process, and the time needed to completely melt the paraffin.
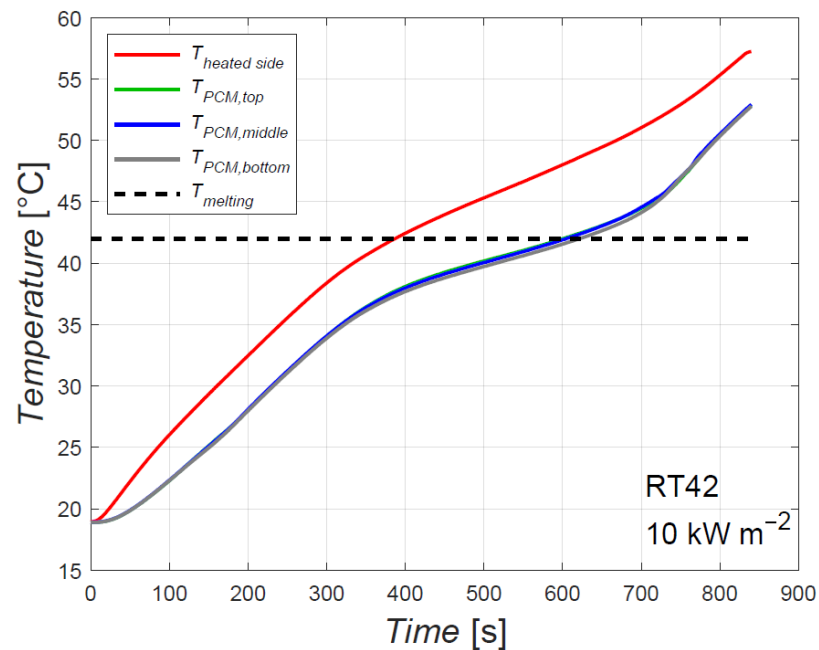
**Figure 5.** Temperature profiles for the paraffin RT42 with an imposed heat flux of 10 kW m$^{-2}$.

**Table 3.** Summary of the experimental results.

|  | $T_i$ [°C] | $T_f$ [°C] | $t_{melt}$ [s] |
|---|---|---|---|
| RT42, *HF* = 10 kW m$^{-2}$ | 18.93 | 56.82 | 833 |
| RT42, *HF* = 15 kW m$^{-2}$ | 19.47 | 62.18 | 575 |
| RT42, *HF* = 20 kW m$^{-2}$ | 20.28 | 66.86 | 441 |
| RT55, *HF* = 10 kW m$^{-2}$ | 19.25 | 67.85 | 1107 |
| RT55, *HF* = 15 kW m$^{-2}$ | 19.99 | 73.37 | 749 |
| RT55, *HF* = 20 kW m$^{-2}$ | 20.09 | 78.38 | 578 |
| RT64HC, *HF* = 10 kW m$^{-2}$ | 20.81 | 77.30 | 1434 |
| RT64HC, *HF* = 15 kW m$^{-2}$ | 20.53 | 82.80 | 936 |
| RT64HC, *HF* = 20 kW m$^{-2}$ | 20.38 | 88.31 | 713 |

An overview of the melting front is given in Figure 6, which reports pictures at different times taken from the glass window in front of the test module for the paraffin RT42 with an imposed heat flux of 10 kW m$^{-2}$. The figure demonstrates that the melting front propagates almost vertically, i.e., the tested porous matrix tends to limit the natural convection of the PCM embedded inside. Due to volume variation during the phase transition from solid to liquid conditions, the melted liquid paraffin coming from the heated side tends to overcome the still solid paraffin on the top part, and this phenomenon is responsible for the slight inclination of the melting front as time goes by. Similar conclusions can be drawn for the other paraffin waxes and heat fluxes.

subsectionEffect of the Heat Flux on the Heating Process

The effect of the heat flux on the heating process is highlighted in Figure 7. The figure proposes the case for the paraffin with a melting temperature of 42 °C, but similar conclusions can be drawn for the other paraffins, whose data can be extrapolated from Table 3. Since experimental tests at different heat fluxes were carried out on different days, with consequently different ambient temperatures, the difference between the temperature of the heated side (average value between the six values recorded by the six thermocouples) and the ambient temperature is considered in the *y*-axis instead of the temperature itself, allowing a better comparison for different initial temperatures.
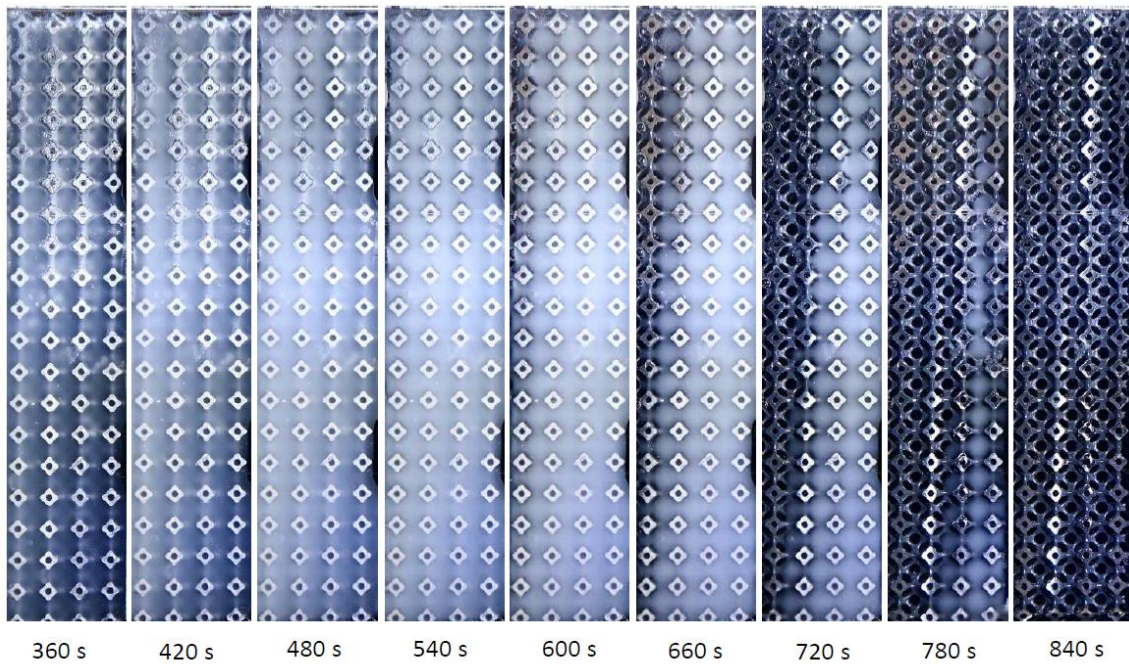
**Figure 6.** Melting fronts for the paraffin RT42 with an imposed heat flux of 10 kW m$^{-2}$.
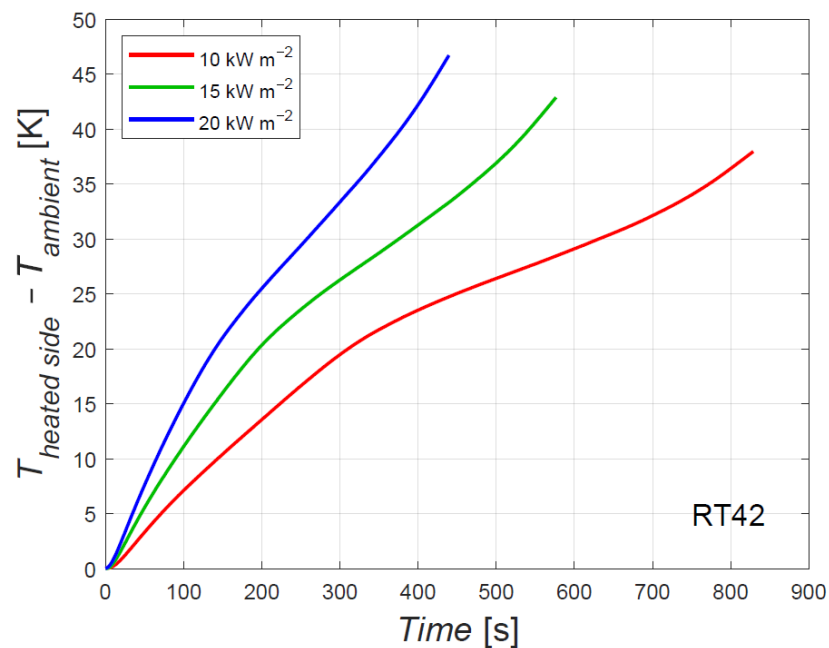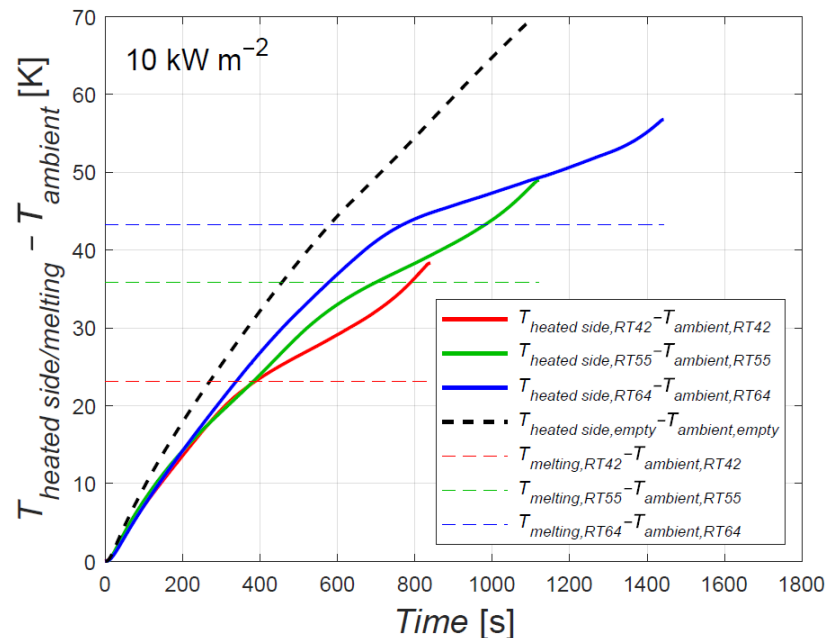


**Figure 7.** Temperature difference profiles for the paraffin RT42 at different heat fluxes.

As expected, the higher the heat flux, the higher the temperature reached by the heated side at the end of the melting process of the paraffin embedded in the porous matrix, and the shorter the time needed to completely melt the paraffin.

*5.3. Effect of the Melting Temperature of the Paraffin on the Heating Process*

The effect of the melting temperature is reported in Figure 8, which reports the difference between the temperature of the heated side and the ambient temperature on the *y*-axis versus time with an imposed heat flux of 10 kW m$^{-2}$ for the three different tested paraffin waxes. Figure 8 also reports the difference between the melting temperature of the considered paraffin and the correspondent ambient temperature. As a reference case,

the case with the porous matrix without any paraffin was considered, and it represents the black dotted line in the figure. The figure reveals that the effect of the PCM in the porous matrix is always positive compared to the case without paraffin, lowering the temperature of the heated side even if the paraffin has low thermal conductivity. The benefit is enhanced as soon as the phase change process starts.



**Figure 8.** Temperature difference profiles at 10 kW$^{-2}$ for different paraffins.

The figure also permits highlighting the effect of the melting temperature on the heating process. As expected, the higher the melting temperature, the longer the time needed to completely melt the paraffin since a longer time is needed to start the phase change process. Furthermore, a proper choice of the melting temperature of the paraffin should be carried out in a real case of a heat transfer device that implements such a technique: the melting temperature depends on the time during which the heat transfer device is supposed to work. For this porous matrix with an imposed heat flux of 10 kW m$^{-2}$, the paraffin RT42 should be preferred for a time shorter than about 830 s, the paraffin RT55 for a time between 830 and 1120 s, whereas the paraffin RT64HC for a longer time. Similar results can be found with the other imposed heat fluxes.

*5.4. Comparison against Metal Foams*

A comparison between the results of the modified BCC structure and metal foams is reported here. Two metal foams were chosen for the comparison: the first one is a Duocel® aluminum foam with five pores per linear inch and a porosity of 92%, whose data will later be referred to as Al-5-8.0 (data from Diani and Campanale [24]). The second Duocel® foam is made of copper with ten pores per linear inch and a porosity of 93.3%, whose data will later be referred to as Cu-10-6.7 (data from Diani and Rossetto [28]). No data were available for a copper foam with five pores per linear inch, which correspond to a pore size of about 5 mm, equal to the edge of the base cell of the modified BCC structure here proposed. However, the number of pores per inch does not affect the thermal response of structures having the same porosity, as highlighted by Mancin et al. [10] and by Diani and Campanale [24].

Figure 9a reports the temperature of the heated side at the end of the melting process for the three structures as a function of the heat flux for the paraffin with a characteristic melting temperature of 42 °C. The worst thermal performance is shown by the aluminum foam. The modified BCC structure, even if it has the lowest parent thermal conductivity

($175$ W m$^{-1}$ K$^{-1}$ for the modified BCC structure vs. $390$ W m$^{-1}$ K$^{-1}$ for the copper foam and $220$ W m$^{-1}$ K$^{-1}$ for the aluminum foam), shows the best thermal performance, i.e., the lowest temperatures at the end of the melting process. This can be mainly attributed to its lower porosity compared to the other two structures, coupled with the particular structure of the BCC matrix, which augments the tortuosity compared to metal foams, globally enhancing the effective thermal conductivity of the PCM/porous matrix block. As a result, the modified BCC structure outperforms the proposed structures.
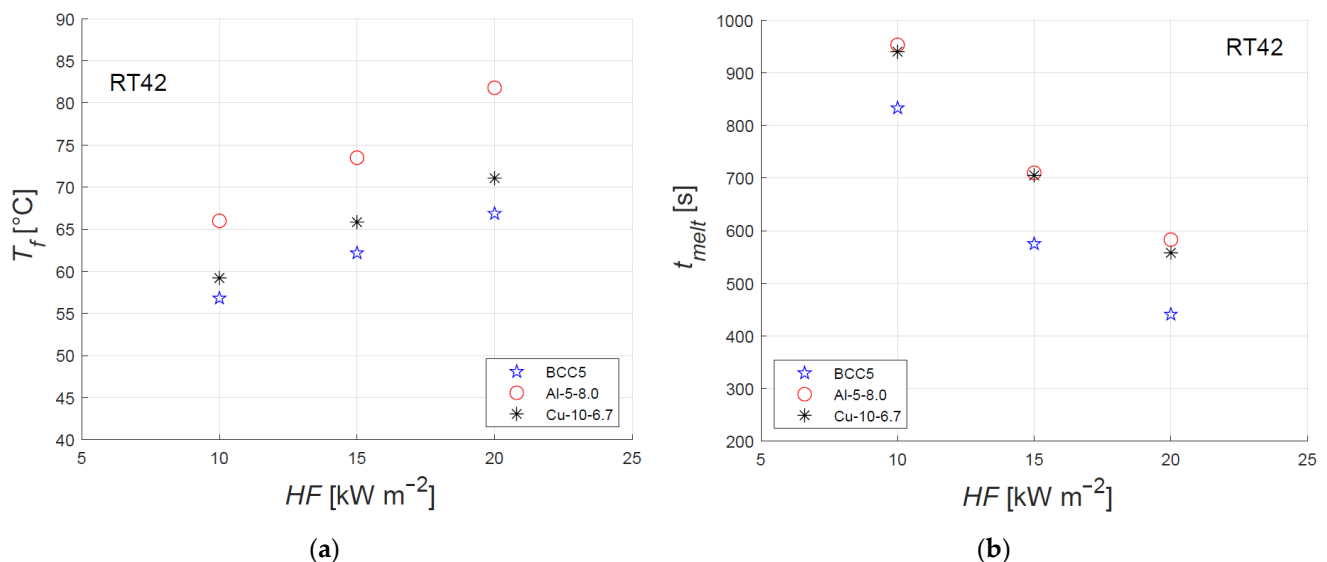


**Figure 9.** (**a**) Temperature reached by the heated side at the end of the melting process for different structures (case with RT42); (**b**) time needed to completely melt the paraffin for different structures (case with RT42).

The lower porosity means a lower amount of phase change material embedded inside. Figure 9b shows the time needed to completely melt the paraffin embedded within the three different structures. All the initial temperatures do not differ more than 3 K. As expected, the modified BCC structure needs a shorter time to completely melt the paraffin. However, it is interesting to highlight that, even if embeds a lower amount of PCM, the modified BCC structure outperforms the other two tested structures. This does not mean that the endless lowering of the porosity leads to better performance because lowering the porosity also means a lower effect of the latent heat of the PCM: there will be an optimum porosity that balances the effect of the thermal conductivity and of the latent heat of the PCM. Future work will investigate this aspect.

## 6. Conclusions

This paper explored the coupling between a porous matrix and phase change materials. The porous matrix was made by additive manufacturing, and it is made of AlSi$_{10}$Mg, which is an aluminum alloy with a thermal conductivity of $175$ W m$^{-1}$ K$^{-1}$. Modified BCC cells with an edge of 5 mm, form the matrix. Three different paraffins, having different melting temperatures (42, 55, and 64 °C), were used as phase change material. First of all, the thermal conductivities and diffusivities of the three PCMs and of AlSi$_{10}$Mg were measured with the hot disk transient plane source (TPS) method.

The entire structure was laterally heated with an electrical heater for the phase change tests, applying three different heat fluxes: 10, 15, and 20 kW m$^{-2}$. The experimental results were given in terms of the temperature profile of both the heated side and of the paraffin during the heating process. The main findings are the following:

- The melting front is almost parallel to the heating side, and this is confirmed by the temperatures of the PCM at different heights, which are approximately equal at each time;

- The higher the heat flux, the higher the temperature of the heated side, and the shorter the time needed to completely melt the paraffin;
- Compared to the case without PCM, adding paraffin leads to lower temperatures of the heated side for all the heating processes; the benefit is increased when the phase change process starts;
- A proper selection of the melting temperature is to be carried out in the case of a heat transfer device, and it depends on the time during which the device is supposed to work;
- The comparison against an aluminum foam and a copper foam revealed that the modified BCC structure outperforms the considered structures under the same working conditions.

# References

1. Kwon, B.; Liebenberg, L.; Jacobi, A.M.; King, W.P. Heat transfer enhancement of internal laminar flows using additively manufactured static mixers. *Int. J. Heat Mass Transf.* **2019**, *137*, 292–300. [CrossRef]
2. Rastan, H.; Abdi, A.; Hamawandi, B.; Ignatowicz, M.; Meyer, J.P.; Palm, B. Heat transfer study of enhanced additively manufactured minichannel heat exchangers. *Int. J. Heat Mass Transf.* **2020**, *161*, 120271. [CrossRef]
3. Unger, S.; Beyer, M.; Pietruske, H.; Szalinki, L.; Hampel, U. Air-side heat transfer and flow characteristics of additively manufactured finned tubes in staggered arrangement. *Int. J. Therm. Sci.* **2021**, *161*, 106752. [CrossRef]
4. Fok, S.; Shen, W.; Tan, F. Cooling of portable hand-held electronic devices using phase change materials in finned heat sinks. *Int. J. Therm. Sci.* **2010**, *49*, 109–117. [CrossRef]
5. Baby, R.; Balaji, C. Thermal optimization of PCM based pin fin heat sinks: An experimental study. *Appl. Therm. Eng.* **2013**, *54*, 65–77. [CrossRef]
6. Lafdi, K.; Mesalhy, O.; Shaikh, S. Experimental study on the influence of foam porosity and pore size on the melting of phase change materials. *J. Appl. Phys.* **2007**, *102*, 083549. [CrossRef]
7. Zhou, D.; Zhao, C. Experimental investigations on heat transfer in phase change materials (PCMs) embedded in porous materials. *Appl. Therm. Eng.* **2011**, *31*, 970–977. [CrossRef]
8. Li, W.; Qu, Z.; He, Y.; Tao, W. Experimental and numerical studies on melting phase change heat transfer in open-cell metallic foams filled with paraffin. *Appl. Therm. Eng.* **2012**, *37*, 1–9. [CrossRef]
9. Hu, X.; Patnaik, S.S. Modeling phase change material in micro-foam under constant temperature condition. *Int. J. Heat Mass Transf.* **2014**, *68*, 677–682. [CrossRef]
10. Mancin, S.; Diani, A.; Doretti, L.; Hooman, K.; Rossetto, L. Experimental analysis of phase change phenomenon of paraffin waxes embedded in copper foams. *Int. J. Therm. Sci.* **2015**, *90*, 79–89. [CrossRef]
11. Joshi, V.; Rathod, M.K. Thermal performance augmentation of metal foam infused phase change material using a partial filling strategy: An evaluation for fill height ratio and porosity. *Appl. Energy* **2019**, *253*, 113621. [CrossRef]
12. Iasiello, M.; Mameli, M.; Filippeschi, S.; Bianco, N. Metal foam/PCM melting evolution analysis: Orientation and morphology effects. *Appl. Therm. Eng.* **2021**, *187*, 116572. [CrossRef]
13. Sinn, C.; Wentrup, J.; Pesch, G.R.; Thöming, J.; Kiewidt, L. Structure-heat transport analysis of periodic open-cell foams to be used as catalyst carriers. *Chem. Eng. Res. Des.* **2021**, *166*, 209–219. [CrossRef]

14. Lucci, F.; Della Torre, A.; Montenegro, G.; Kaufmann, R.; Eggenschwiler, P.D. Comparison of geometrical, momentum and mass transfer characteristics of real foams to Kelvin cell lattices for catalyst applications. *Int. J. Heat Mass Transf.* **2017**, *108*, 341–350. [CrossRef]

15. Sun, M.; Yang, L.; Hu, C.; Zhao, J.; Tang, D.; Song, Y. Simulation of forced convection heat transfer in Kelvin cells with op-timized skeletons. *Int. J. Heat Mass. Transf.* **2021**, *165*, 120637. [CrossRef]

16. Moon, C.; Kim, H.D.; Kim, K.C. Kelvin-cell-based metal foam heat exchanger with elliptical struts for low energy consumption. *Appl. Therm. Eng.* **2018**, *144*, 540–550. [CrossRef]

17. Sun, M.; Li, M.; Hu, C.; Yang, L.; Song, Y.; Tang, D.; Zhao, J. Comparison of forced convective heat transfer between pillar and real foam structure under high Reynolds number. *Appl. Therm. Eng.* **2021**, *182*, 116130. [CrossRef]

18. Kuruneru, S.; Saha, S.; Sauret, E.; Gu, Y. Transient heat transfer and non-isothermal particle-laden gas flows through porous metal foams of differing structure. *Appl. Therm. Eng.* **2019**, *150*, 888–903. [CrossRef]

19. Yao, Y.; Wu, H. Pore-scale simulation of melting process of paraffin with volume change in high porosity open-cell metal foam. *Int. J. Therm. Sci.* **2019**, *138*, 322–340. [CrossRef]

20. Krishnan, S.; Murthy, J.Y.; Garimella, S.V. Direct Simulation of Transport in Open-Cell Metal Foam. *J. Heat Transf.* **2006**, *128*, 793–799. [CrossRef]

21. Krishnan, S.; Garimella, S.V.; Murthy, J.Y. Simulation of Thermal Transport in Open-Cell Metal Foams: Effect of Periodic Unit-Cell Structure. *J. Heat Transf.* **2008**, *130*, 024503. [CrossRef]

22. Ferfera, R.S.; Madani, B.; Serhane, R. Investigation of heat transfer improvement at idealized microcellular scale for metal foam incorporated with paraffin. *Int. J. Therm. Sci.* **2020**, *156*, 106444. [CrossRef]

23. Zhao, C. Review on thermal transport in high porosity cellular metal foams with open cells. *Int. J. Heat Mass Transf.* **2012**, *55*, 3618–3632. [CrossRef]

24. Diani, A.; Campanale, M. Transient melting of paraffin waxes embedded in aluminum foams: Experimental results and mod-elling. *Int. J. Therm. Sci.* **2019**, *144*, 119–128. [CrossRef]

25. Rubitherm Technologies GmbH. Available online: https://www.rubitherm.eu/en/index.php/productcategory/organische-pcm-rt (accessed on 3 May 2021).

26. Gustafsson, S.E. Transient plane source techniques for thermal conductivity and thermal diffusivity measurements of solid materials. *Rev. Sci. Instrum.* **1991**, *62*, 797–804. [CrossRef]

27. Gustavsson, M.; Karawacki, E.; Gustafsson, S.E. Thermal conductivity, thermal diffusivity, and specific heat of thin samples from transient measurements with hot disk sensors. *Rev. Sci. Instrum.* **1994**, *65*, 3856–3859. [CrossRef]

28. Diani, A.; Rossetto, L. Melting of PCMs Embedded in Copper Foams: An Experimental Study. *Materials* **2021**, *14*, 1195. [CrossRef] [PubMed]